ADVANCED FUNCTIONAL MATERIALS

Supporting Information

for *Adv. Funct. Mater.,* DOI: 10.1002/adfm.202211805

Sn-O Dual-Substituted Chlorine-Rich Argyrodite Electrolyte with Enhanced Moisture and Electrochemical Stability

*Guoyao Li, Shaoping Wu, Hongpeng Zheng, Yu Yang, Jingyu Cai, Hong Zhu, Xiao Huang, Hezhou Liu, and Huanan Duan**

Supporting Information

Title: Sn-O Dual-substituted Chlorine-rich Argyrodite Electrolyte with Enhanced Moisture and Electrochemical Stability

*Guoyao Li[a], Shaoping Wu[a], Hongpeng Zheng[a], Yu Yang[b], Jingyu Cai[a], Hong Zhu[b], Xiao Huang[c], Hezhou Liu[a], Huanan Duan[a]**

[a]G. Li, S. W, H. Zheng, J. Cai, H. Liu, H. Duan*
State Key Laboratory of Metal Matrix Composites, School of Materials Science and Engineering, Shanghai Jiao Tong University, Shanghai 200240, P. R. China
E-mail: hd1@sjtu.edu.cn
[b]Y. Yang, H. Zhu
University of Michigan-Shanghai Jiao Tong University Joint Institute, Shanghai Jiao Tong University, Shanghai 200240, P. R. China
[c]X. Huang
SZU-NUS Collaborative Innovation Center for Optoelectronic Science & Technology, International Collaborative Laboratory of 2D Materials for Optoelectronics Science and Technology of Ministry of Education, Institute of Microscale Optoelectronics, Shenzhen University, Shenzhen 518060, P. R. China

METHODS

Materials synthesis

All preparations and sample treatments were carried out in an argon-filled glove box (O_2 and H_2O < 0.1 ppm) owing to the extreme sensitivity of sulfide electrolytes to oxygen and moisture. The chlorine-rich argyrodites were synthesized via conventional solid-state sintering. Analytical grade precursors, including lithium sulfide (Li_2S, Aladdin, 99.98%), phosphorus pentasulfide (P_2S_5, Meryer, 99%), lithium chloride (LiCl, Aladdin, 99%), and dual-dopant of tin sulfide (SnS_2, Aladdin, 99.5%) and phosphorus pentoxide (P_2O_5, Aladdin, 99.99%), were weighted according to the proper stoichiometric ratio of $Li_{5.4+x}(P_{1-x}Sn_x)(S_{4.4-2x}O_{2x})Cl_{1.6}$ (x = 0, 0.1, 0.2, and 0.3), and each composition was denoted as LPSC, LPSC-10, LPSC-20, and LPSC-30, respectively. For comparison, SnO_2 (Aladdin, 99.9%) was used to replace the dual-dopant of SnS_2 and P_2O_5 according to the same molar amount of Sn and O atoms,

and each corresponding composition was denoted as LPSC-10SnO_2, LPSC-20SnO_2, and LPSC-30SnO_2, respectively. The precursors were hand-ground in an agate mortar and then transferred into Al_2O_3 crucibles, which were sealed in the quartz bottle for the subsequent annealing. The annealing process was done at 470, 500, and 530 °C for 16 hours with a ramping rate of 1 °C min^{-1} and followed by natural cooling to room temperature. The obtained samples were again hand-ground to achieve the reduced particle size for the subsequent tests.

Materials characterization

The chlorine-rich argyrodites were sealed via a Kapton tape and subjected to a powder X-ray diffractometer (Rigaku, Japan, Cu Kα radiation). XRD data were recorded in a 2θ range between 10° and 60° with a step size of 0.02° to investigate the crystal structure. The XRD refinement was done by the Rietveld method using Fullprof. Raman spectroscopy was performed to pinpoint different vibrational modes of ortho-thiophosphate (PS_4^{3-}) as well as Sn- and O- substituted chemical groups for the powder samples sealed in transparent glass with airtight grease. The Raman measurements were taken with a 532 nm incident laser beam by a confocal Raman spectrometer (Renishaw, UK). Morphology of the samples was obtained by a field-emission scanning electron microscope (FE-SEM, Sirion 200, FEI USA) using an airtight transfer vessel. EDX analysis was conducted using an energy dispersive spectroscopy (INCA X-Act, Oxford UK) with an acceleration voltage of 20 kV. X-ray photoelectron spectroscopy (XPS) was carried out in a Thermo Scientific K-Alpha+ spectrometer (ThermoFisher, USA) with monochromatic Al Kα source (1486.6 eV), and the analysis chamber pressure was less than 5 × 10-9 mbar. Charge correction was conducted relative to the C 1s signal of adventitious carbon (284.8 eV).

Electrochemical measurements

The ionic conductivity of the sulfide electrolyte was determined by

electrochemical impedance spectroscopy (EIS) using a Solartron 1260 potentiostat. The as-synthesized powders (0.5 g) were cold-pressed into pellets with a diameter of 14 mm and a thickness of 1.8-2.0 mm using a uniaxial pressure of 235 MPa. EIS was carried out in a frequency range of 5 MHz – 1 Hz at 20 mV with carbon-coated Al foils serving as blocking electrodes. The equivalent circuit (R//CPE)-CPE was employed to fit the EIS plots [1] using ZSimpWin. The total conductivity (σ_{total}) of the sulfide sample pelletized in cold-pressed condition was determined via equation 1:

$$\sigma_{total} = \frac{l}{AR_{total}} \quad \textbf{(1)}$$

Where l and A are the thickness and area, respectively, of the cold-pressed pellet; R_{total} refers to the total resistance of the bulk transport, obtained from the fitting results using the above-mentioned equivalent circuit. The activation energy was determined by EIS measurements in the temperature range of 303-353 K with an interval of 5 K. The value was calculated by the Arrhenius equation as stated in equation 2 [2].

$$\sigma T = \sigma_0 \exp\left(\frac{-E_a}{RT}\right) \quad \textbf{(2)}$$

Where σ is the ionic conductivity as calculated in equation 1, T is the measuring temperature in Kelvin, σ_0 is the pre-exponential factor, and R is the universal gas constant.

To examine the electrochemical stability with lithium, the cold-pressed pellets were assembled into Li|SE|Li symmetric cells for galvanostatic cycling measurements. Two pieces of Li foils (450 μm thick, China Energy Lithium Co., Ltd.) were attached on both sides of the cold-pressed pellet and underwent a 50 MPa pressure to fulfill the intimate interface contact. The galvanostatic cycling was conducted using a cell test system (C2001A, LAND China). For the cyclic voltammetry (CV), the cold-pressed pellets were assembled into Li|SE|SS asymmetric cells with a stainless-steel disk as a working electrode and lithium foil as a counter and reference electrode. The voltage profile vs. Li^+/Li was studied using a CHI600D potentiostat with the range from -0.5 to 5 V at a scan rate of 1 mV s^{-1}.

To fabricate an all-solid-state battery (ASSB), a composite cathode (11 mg) was

employed, consisting of Li_3BO_3-coated $LiNi_{0.8}Mn_{0.1}Co_{0.1}O_2$ (NMC811@LBO) and argyrodite electrolyte with a mass ratio of 70:30. The active mass loading in the composite cathode is 5.0 mg cm^{-2}. NMC811@LBO particles were provided by XTC New Energy Co., Ltd. Here, a 100-mesh stainless steel sieve of customized size was used to ensure the cathode particles were evenly distributed. The composite cathode was added on one side of the cold-pressed pellet and consolidated using a 250 MPa pressure. Then, a piece of Li-In alloy foil was attached to another side of the as-consolidated pellet and underwent a 50 MPa pressure to form a triple-layer battery structure of LiIn|SE|NMC811. The charging-discharging cycling of the ASSBs was conducted with a voltage range of 2.2-3.7 V vs Li-In alloy (equally 2.8-4.3 V vs Li^+/Li) at 38 ± 2 ^oC with a holding pressure of 5 MPa. 1 C equals 188 mA g_{NMC811}^{-1} in this work.

Moisture stability tests

The cold-pressed pellet was exposed to the humid air (50%) at room temperature for 1, 3, and 5 minutes and tempered at 120 ℃ for 1 hour to eliminate the absorbed H_2O. The EIS measurements were carried out after each exposure and the heat treatment. The 5-minute-exposed and heat-treated sample is denoted as 5-HT. 5-HT samples were assembled into symmetric lithium cells to demonstrate the structure and cycling stability. The H_2S gas concentration generated from a 100 mg cold-pressed pellet was monitored via a sensor (Intersense SP100, Hanwei Electronics Group Corporation). Apart from the pelletized sample, a portable electric fan was placed in a 10-liter desiccator to accelerate the gas flow and mixture.

First-principles calculation

DFT calculations were performed within the Vienna Ab initio Simulation Package (VASP) [3] software based on the projector augmented wave (PAW) [4] method. The generalized gradient approximation (GGA) with the Perdew-Burke-Ernzerhof (PBE)

[5] functional was used as the exchange-correlation functional. A plane-wave energy cutoff of 520 eV was used and the Brillouin zone was sampled by a 1 × 2 × 2 gamma-centered k-mesh. The convergence criteria of the energy and force are 1×10^{-5} eV and 0.01 eV/Å, respectively.

The ground state structure of $Li_{5.5}PS_{4.5}Cl_{1.5}$: The initial structure of Li_6PS_5Cl was obtained from the MP database (id: mp-985592). Cl^- substitution at the 4c S^{2-} sites with corresponding changes in the Li^+ concentration was performed in a 2 × 1 × 1 Li_6PS_5Cl supercell. All symmetrically distinctive structures were generated for the $Li_{5.5}PS_{4.5}Cl_{1.5}$ and ordered all these structures using the electrostatic energy criterion implemented in the pymatgen code [6]. Then, the lowest electrostatic energy structure was selected for the DFT relaxation calculation.

The ground state structure of $Li_{5.625}(P_{0.875}Sn_{0.125})(S_{4.25}O_{0.25})Cl_{1.5}$: Sn^{4+} substitution for P^{5+} with corresponding changes in the Li^+ concentration was performed based on the structure of $Li_{5.5}PS_{4.5}Cl_{1.5}$, and we performed a similar electrostatic ordering of the structures. Then, three dual-substituted models were considered to determine the O^{2-} position, as shown in Figure S1, and the structure with the lowest formation energy was selected for the subsequent calculations of hydrolysis reaction energy. The energies of solid phases are based on total electronic energy, and the energies of gaseous species, including H_2O and H_2S, are based on experimental values [7].

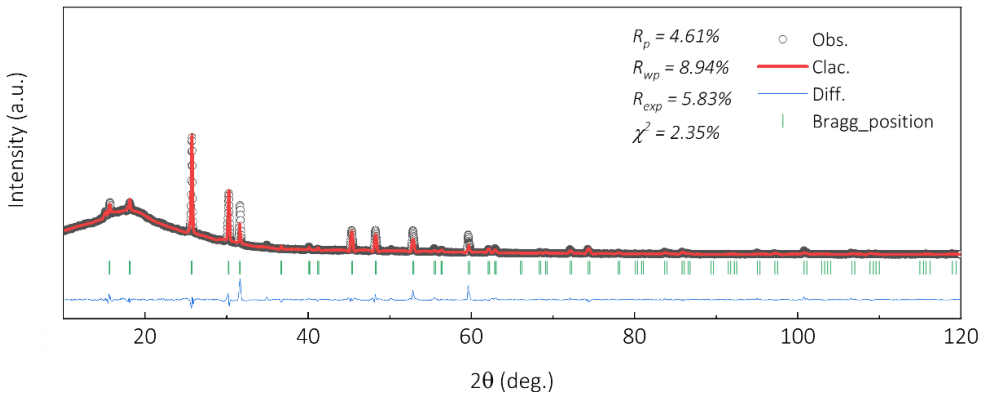

Figure S1 Rietveld refinement of powder X-ray diffraction pattern of $Li_{5.4}PS_{4.4}Cl_{1.6}$ (LPSC) at room temperature.

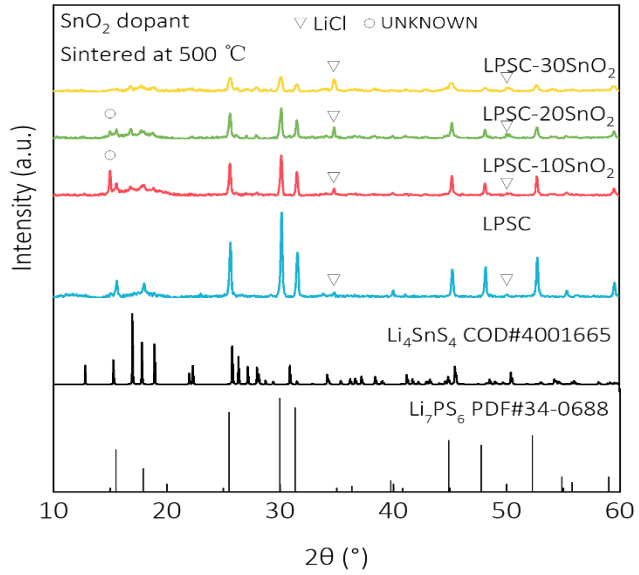

Figure S2 The powder XRD patterns of the sulfide samples sintered at 500 ℃ and employing SnO_2 dopant, the referenced pattern of the secondary phase Li_4SnS_4 (source: Crystallography Open Database), and the standard PDF of the cubic-phase argyrodite sulfide Li_7PS_6.

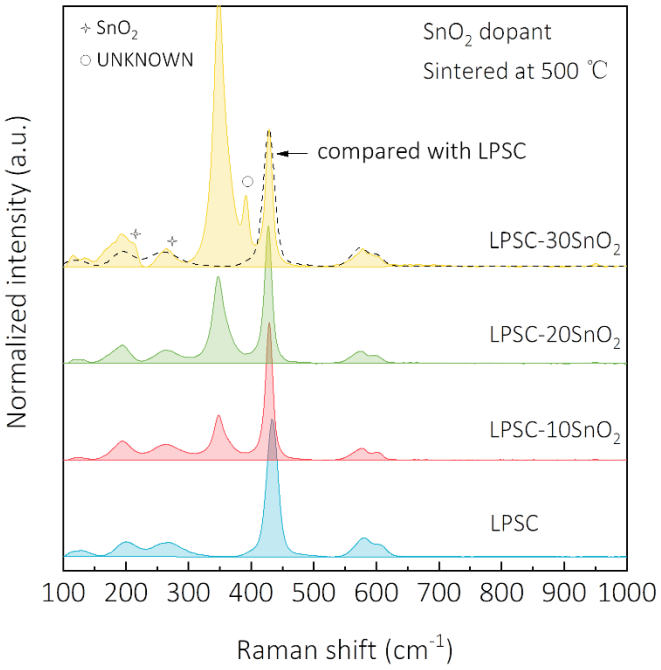

Figure S3 The Raman spectroscopy of the sulfide samples sintered at 500 ℃ and employing SnO_2 dopant.

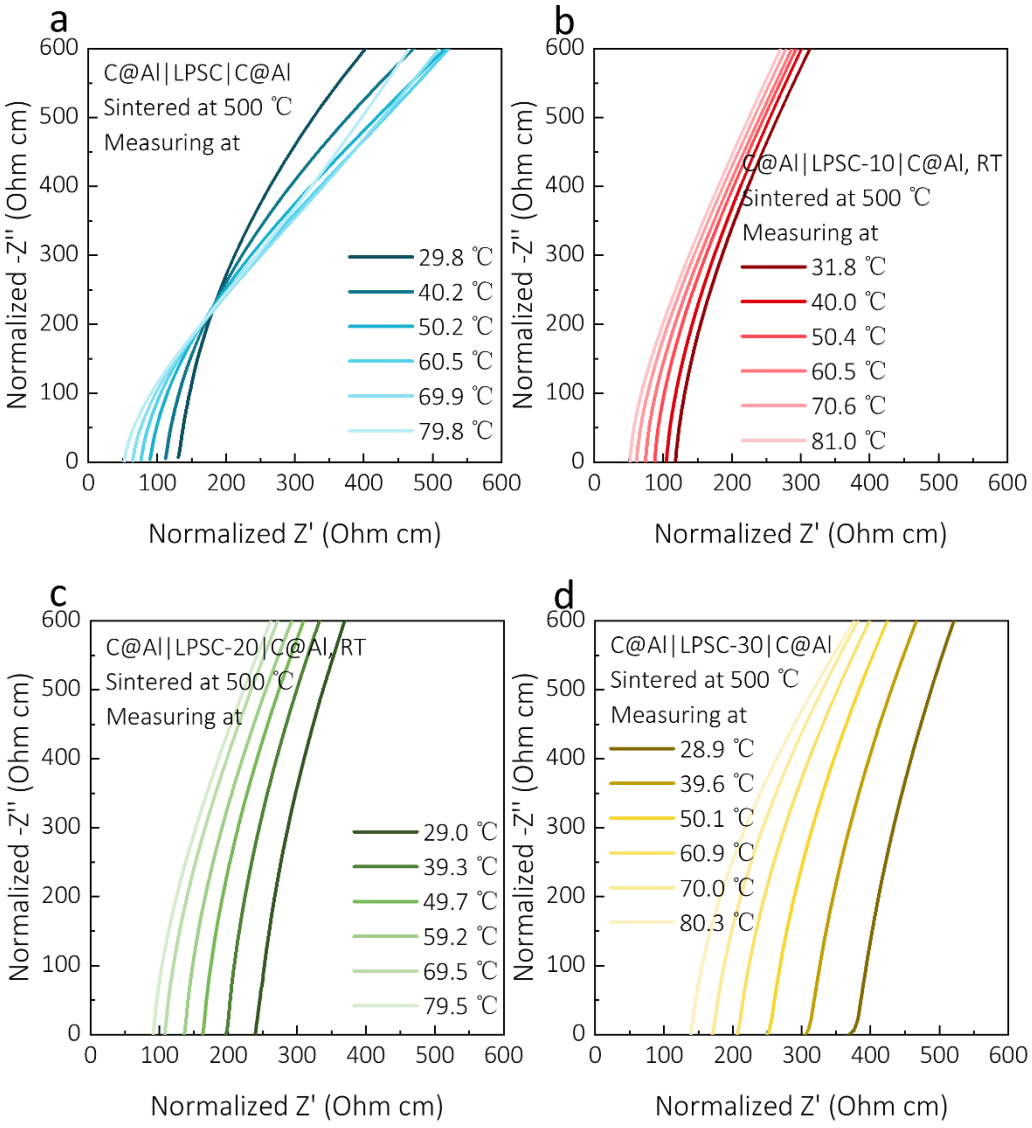

Figure S4 The temperature-dependent EIS plots of the pelletized samples sintered at 500 ℃, measured at a temperature range of 303-353 K with an interval of 5 K (shown with an interval of 10 K), where the impedance is normalized to the respective pellet geometry. (a) LPSC. (b) LPSC-10. (c) LPSC-20. (d) LPSC-30.

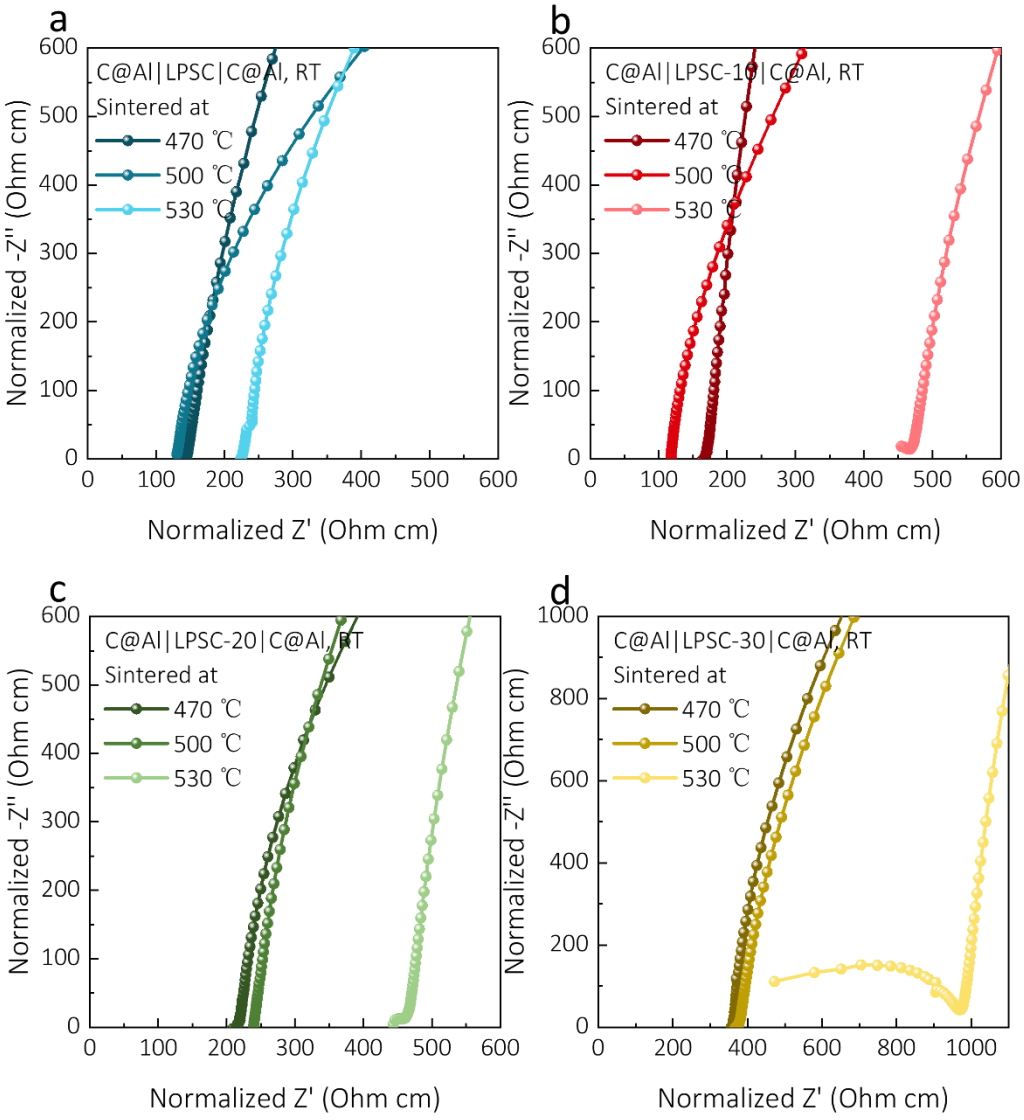

Figure S5 The EIS plots of the pelletized samples sintered at 470, 500, and 530 ℃, measured at ambient temperature, where the impedance is normalized to the respective pellet geometry. (a) LPSC. (b) LPSC-10. (c) LPSC-20. (d) LPSC-30.

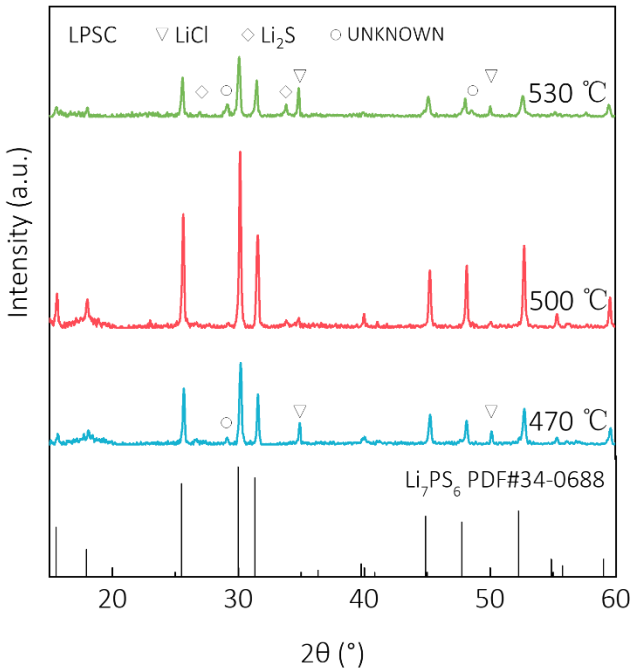

Figure S6 The powder XRD patterns of the unsubstituted LPSC that sintered at 470, 500 ℃, and 530 ℃, and the standard PDF of the cubic-phase argyrodite-type sulfide Li_7PS_6.

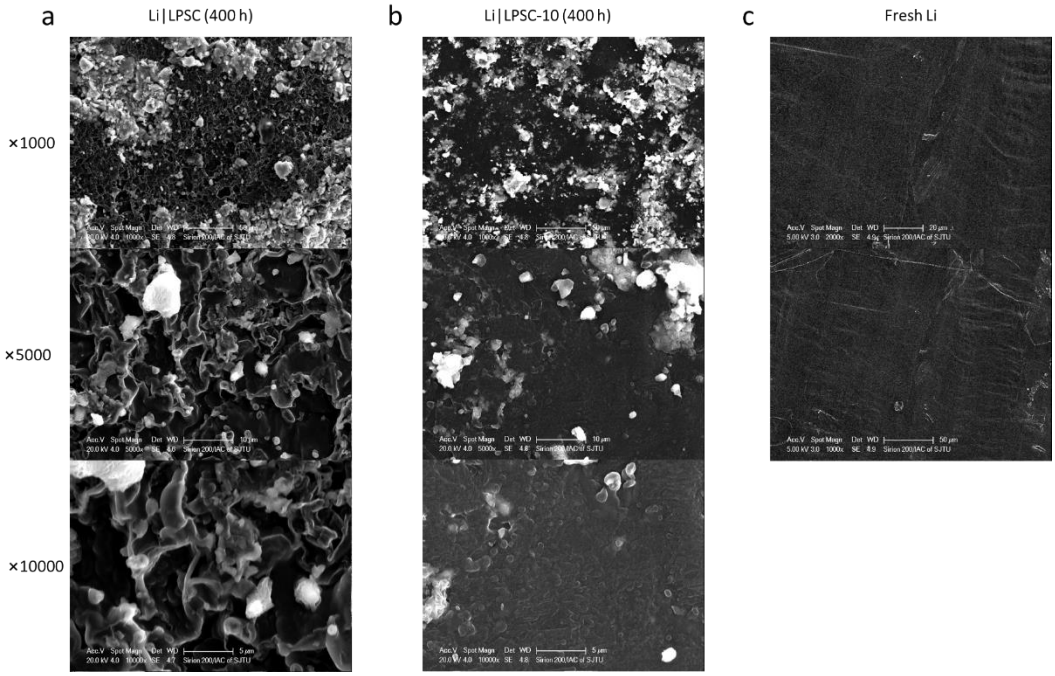

Figure S7 The surficial morphology and element distribution of the lithium foil: (a)

Separated from the Li|LPSC|Li cell after cycling for 400 hours; (b) Separated from the Li|LPSC-10|Li cell after cycling for 400 hours. (c) The uncycled one.

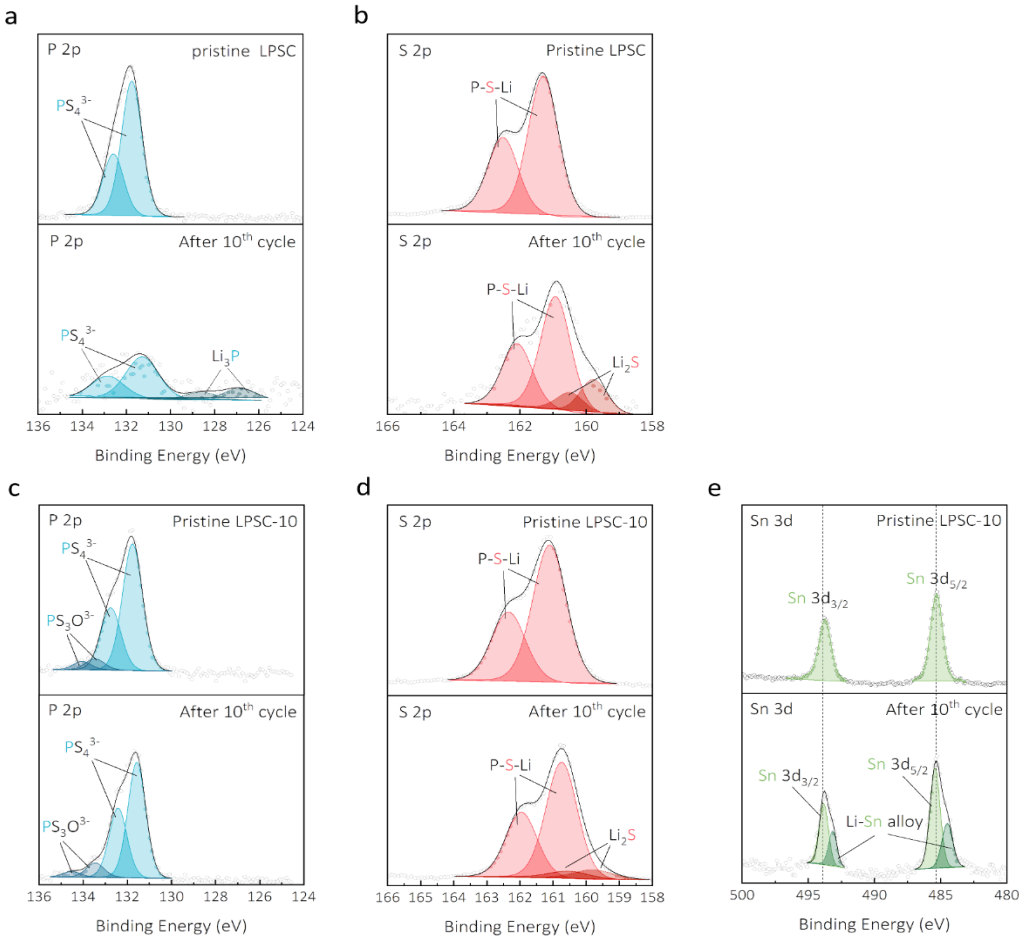

Figure S8 The chemical information of the lithium and electrolyte interface from 20-hour-cycled symmetric lithium cells, which were cycled at 0.5 mA cm^{-2} and 65 °C. XPS spectra: (a) P 2p and (b) S 2p in the Li|LPSC|Li cell; (c) P 2p, (d) S 2p and (e) Sn 3d in the Li|LPSC-10|Li cell.

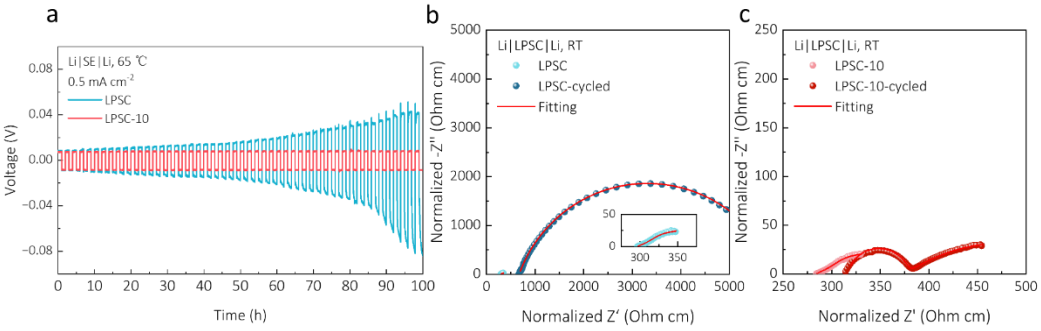

Figure S9 (a) The voltage profile of the symmetric lithium cells cycled at 0.5 mA cm^{-2} and 65 ℃; The EIS plots before and after 100-hour cycling for (b) Li|LPSC|Li and (c) Li|LPSC-10|Li.

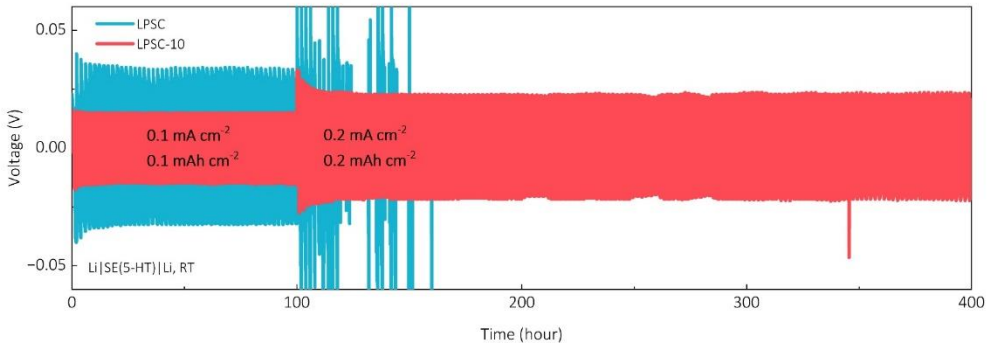

Figure S10 The voltage profile of the Li symmetric cells assembled with the air-exposed and heat-treated sulfide samples.

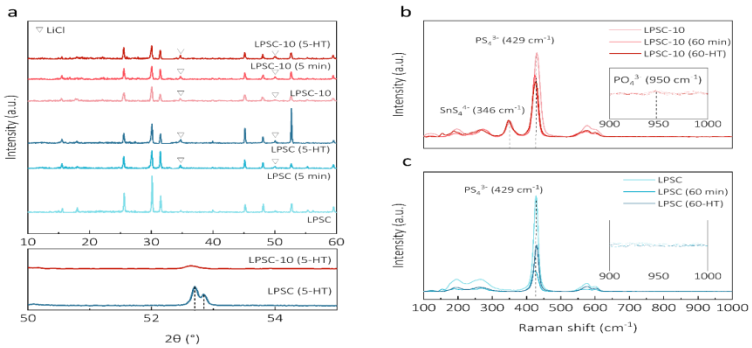

Figure S11 Characterization of the chemical composition and structure of the sulfide samples that were exposed to the humid air (50%) and tempered at 120 ℃ for 1 hour. (a) The powder XRD patterns of the samples. (b-c) The Raman spectroscopy of the samples.

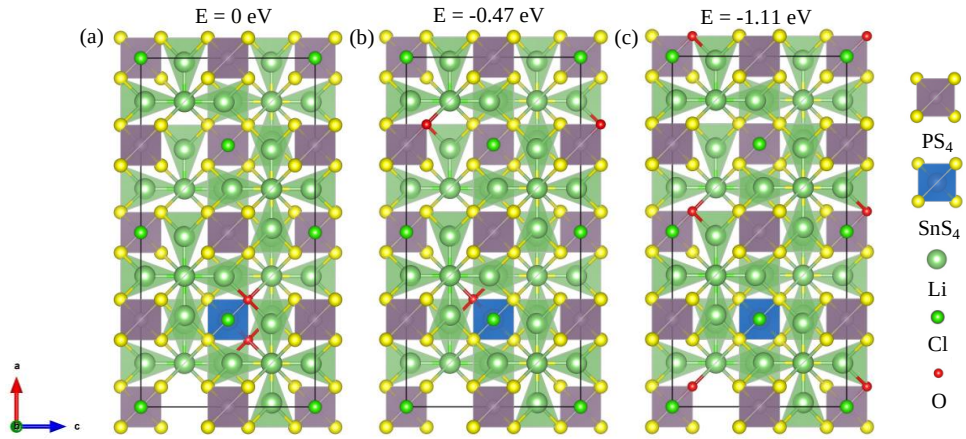

Figure S12 The position of substituted O^{2-} and corresponding formation energies in $Li_{5.625}(P_{0.875}Sn_{0.125})(S_{4.25}O_{0.25})Cl_{1.5}$ supercell. (a) Two O^{2-} occupy the same SnS_4^{4-} tetrahedron; (b) One O^{2-} occupy SnS_4^{4-} tetrahedron and the other O occupy PS_4^{3-} tetrahedron; (c) Two O^{2-} occupy different PS_4^{3-} tetrahedron.

Table S1 Rietveld refinement of powder X-ray diffraction pattern of $Li_{5.4}PS_{4.4}Cl_{1.6}$ (LPSC) at room temperature.

Atom	Wyckoff	x/*a*	y/*b*	z/*c*	Occ.
Li1	48*h*	0.32685	0.0132	0.67315	0.457
P1	4*b*	0	0	0.5	1
S1	4*a*	0	0	1	0.337
Cl1	4*a*	0	0	1	0.663
S2	4*d*	0.25	0.25	0.75	0.141
Cl2	4*d*	0.25	0.25	0.75	0.859
S3	16*e*	0.1198	-0.1198	0.6198	1

Space group: F -4 3 M. a = 9.797 Å. R_p = 4.61%, R_{wp} = 8.94%, R_{exp} = 5.83%, χ^2 =2.35%.

Table S2 Literature overviews of galvanostatic cycling conditions on lithium plating and stripping in sulfide-based symmetric cells.

Ref	Electrolyte	Measuring Temperature (°C)	Critical Current Density (mA cm^{-2})	Cycling Current Density (mA cm^{-2})	Cut-off Capacity (mAh cm^{-2})	Cycling Time (h)
This work	LPSC-SnO	RT	1.2	0.25 0.5	0.25 0.5	200 200

[8]	LPSB-ZnO	RT	0.78	0.78	0.39	140
[9]	LPSB-O	RT	0.89	0.4	0.2	340
[10]	LPSC-O	RT	-	0.4	0.2	150
[11]	LPSI-SnO	RT	0.75	0.2	0.1	180
[12]	LPSI-In	RT	-	0.1	0.1	1000
[13]	LPS-NbO	RT	-	0.1	0.1	100
[14]	LiH_2PO_4| LGPS	RT	-	0.1	0.05	950

Supplementary References:

[1] M. A. Kraft, S. Ohno, T. Zinkevich, R. Koerver, S. P. Culver, T. Fuchs, A. Senyshyn, S. Indris, B. J. Morgan, W. G. Zeier, *Journal of the American Chemical Society* **2018**, 140, 16330.

[2] a) P. Adeli, J. D. Bazak, K. H. Park, I. Kochetkov, A. Huq, G. R. Goward, L. F. Nazar, *Angew Chem Int Ed Engl* **2019**, 58, 8681; b) A. Baktash, J. C. Reid, T. Roman, D. J. Searles, *npj Computational Materials* **2020**, 6, 162.

[3] G. Kresse, J. Furthmüller, *Physical Review B* **1996**, 54, 11169.

[4] P. E. Blöchl, *Physical Review B* **1994**, 50, 17953.

[5] J. P. Perdew, K. Burke, M. Ernzerhof, *Physical Review Letters* **1996**, 77, 3865.

[6] S. P. Ong, W. D. Richards, A. Jain, G. Hautier, M. Kocher, S. Cholia, D. Gunter, V. L. Chevrier, K. A. Persson, G. Ceder, *Computational Materials Science* **2013**, 68, 314.

[7] M. W. Chase, Jr., *NIST-JANAF thermochemical tables, monograph 9*, American Chemical Society, Washington DC **1998**.

[8] T. Chen, L. Zhang, Z. Zhang, P. Li, H. Wang, C. Yu, X. Yan, L. Wang, B. Xu, *ACS Applied Materials & Interfaces* **2019**, 11, 40808.

[9] Z. Zhang, L. Zhang, X. Yan, H. Wang, Y. Liu, C. Yu, X. Cao, L. van Eijck, B. Wen, *Journal of Power Sources* **2019**, 410-411, 162.

[10] L. Peng, S. Chen, C. Yu, C. Wei, C. Liao, Z. Wu, H.-L. Wang, S. Cheng, J. Xie, *ACS Applied Materials & Interfaces* **2022**, 14, 4179.

[11] T. Chen, D. Zeng, L. Zhang, M. Yang, D. Song, X. Yan, C. Yu, *Journal of Energy Chemistry* **2021**, 59, 530.

[12] Z. Jiang, H. Peng, Y. Liu, Z. Li, Y. Zhong, X. Wang, X. Xia, C. Gu, J. Tu, *Advanced Energy Materials* **2021**, 11, 2101521.

[13] N. Ahmad, L. Zhou, M. Faheem, M. K. Tufail, L. Yang, R. Chen, Y. Zhou, W. Yang, *ACS Applied Materials & Interfaces* **2020**, 12, 21548.

[14] Z. Zhang, S. Chen, J. Yang, J. Wang, L. Yao, X. Yao, P. Cui, X. Xu, *ACS Applied Materials & Interfaces* **2018**, 10, 2556.